Advanced Engineering Materials

ADVANCED ENGINEERING MATERIALS
www.aem-journal.com

RESEARCH ARTICLE OPEN ACCESS

Enhanced Ultrasound Transmission Through Aberration Layers Using Space-Coiling Acoustic Metamaterials

Maral Ghanami[1] | Hengzhe Ren[2] | Erqian Dong[2] | Ashkan Ghanbarzadeh-Dagheyan[3] | Chen Shen[1]

[1]Department of Mechanical Engineering, Rowan University, Glassboro, New Jersey, USA | [2]Department of Mechanical Engineering, The University of Hong Kong, Hong Kong, China | [3]Biomedical Photonic Imaging (BMPI) Group, University of Twente, Enschede, The Netherlands

Correspondence: Erqian Dong (eqdong@hku.hk) | Ashkan Ghanbarzadeh-Dagheyan (a.dagheyan@utwente.nl) | Chen Shen (shenc@rowan.edu)

Received: 30 December 2025 | **Revised:** 16 July 2026 | **Accepted:** 22 July 2026

Keywords: acoustics | impedance matching | metamaterial | ultrasound

ABSTRACT

Ultrasound is widely used in medical imaging and therapy. Yet its performance is limited by layers such as the skull or calcified tissue that exhibit an impedance mismatch with the background medium. As a result, wave energy scatters, phase distorts, and overall transmission decrease. To address this, we explore a space-coiling metamaterial that can enhance transmission through aberration layers. The coiled-path design is optimized based on geometric parameters. Finite element simulations demonstrate enhanced transmission through an aberration layer near 4 MHz with water as the background medium. Further analysis shows negative effective properties, which could serve as a complementary layer. To validate this design, a scaled-up prototype was fabricated using fused-silica microfabrication and experimentally tested in a water tank. The measured transmission spectrum shows an enhancement around 450 kHz, matching the expected frequency shift due to geometric scaling. The experimental results exhibit agreement with the numerical predictions, confirming that the enhancement mechanisms, resonant tunneling, and impedance compensation remain effective across different scales. These findings show the potential of space-coiling metamaterials to improve ultrasound transmission through impedance-mismatched layers and support practical implementation. Future work will focus on further experimental validation and integration of such structures into ultrasound systems, including linear-array probes.

1 | Introduction

Ultrasound waves are widely used in different biomedical applications, ranging from ultrasound imaging and treatment to on-chip particle and cell manipulations [1–3]. Compared with other approaches such as optical and magnetic methods, the acoustic waves carry much less energy and are therefore safer, with better biocompatibility while maintaining good penetration depth [4–6]. As such, they have been established as an indispensable tool in medicine and widely adopted in diverse applications. On the other hand, the performance of ultrasound imaging and treatment relies on efficiently delivering the acoustic energy through heterogeneous biological media. In many scenarios, however, the transmission efficiency is compromised due to the existence of aberration layers, which not only distort the phases of the waves but also reduce the overall transmitted energy through them because of backscattering and impedance mismatch [6–9]. For example, transcranial ultrasound imaging of cerebral blood vessels is often limited by the skull's strong attenuation and wavefront distortion [10, 11]. Similarly, therapeutic and diagnostic applications, such as targeted neuromodulation or real-time brain monitoring, are hindered by the skull's high acoustic impedance, which results in poor ultrasound transmission and compromised energy focusing [1]. In addition to challenges posed by skull aberration, recent blood-flow imaging techniques, such as echoPIV, also suffer from the shadow artifacts caused by highly calcified plaques [12, 13].

Several methods have been proposed to overcome the distortion imposed by aberration layers. One widely reported method is to use holographic plates, which can be designed and evaluated efficiently using projection techniques that reconstruct 3D acoustic fields with high accuracy and reduced aberrations. However, this method only corrects the phase and does not fundamentally enhance the transmission [14–16]. Another approach is to utilize impedance-matching layers to eliminate resonance shifts and broaden the transmission bandwidth [17–20]. Additionally, impedance-matching layers can significantly enhance radiation efficiency by mitigating power reflection at the boundary between the human skin and the surrounding air, thereby improving the overall transmission performance [21]. While effective, these matching layers typically do not exhibit high adjustability and are difficult to be tailored to accommodate different scenarios [22].

Another emerging tool is acoustic metamaterials, which are artificially engineered materials that exhibit exotic properties not found in nature such as negative density and bulk modulus [23, 24]. In this way, acoustic metamaterials enable unique interactions with waves, which have been shown to enhance transmission through the layers [4, 25, 26]. For instance, one approach involves using complementary acoustic metamaterials composed of unit cells made from membranes and open-ended side branches. These structures exhibit negative material parameters, enabling them to cancel out aberrating layers and significantly reduce acoustic field distortion [27]. Various resonant and phase-engineered acoustic metamaterial strategies have been explored to enhance ultrasound transmission, improve absorption, broaden bandwidth, and achieve advanced wavefront control [5, 6, 28–32]. While these approaches demonstrate clear benefits for acoustic propagation through complex media, their practical use remains constrained by the fabrication complexity required for precise structural control.

Among the various approaches to metamaterial design, the concept of space-coiling metamaterials has garnered significant attention [33, 34]. Space-coiling metamaterials exploit the concept of folding the propagation path of sound waves within a compact structure, effectively increasing the acoustic path length without increasing the physical dimensions of the material [35, 36]. This coiled design allows for tuning of the operational frequency and acoustic properties, offering greater flexibility in performance. Moreover, since the channels are of uniform size and do not involve curved geometries, they help reduce fabrication complexity, making them more practical for real-world applications [37]. Compared with other metamaterial-based techniques such as membrane metamaterials, the properties of space-coiling metamaterials primarily rely on their geometric configurations. This strong dependence on geometry results in more consistent acoustic performance, as the uniform structural design enhances reproducibility and stability. In contrast, membrane metamaterials often suffer from nonuniform boundary conditions, which can lead to unpredictable behavior. Recent advancements in space-coiling metamaterials have demonstrated that systematic design strategies can be employed to tailor broadband transmission characteristics by optimizing the geometry and arrangement of coiled pathways, enabling efficient manipulation of wave propagation over a wide frequency range [17].

Acoustic metamaterials allow us to steer sound waves by carefully designing their internal structures, essentially endowing them with custom properties such as effective density or bulk modulus. Several architectures have been proposed, from space-coiling paths that delay sound to structures that act like the opposite of a perfect mirror, helping waves pass through barriers. Nevertheless, applying these techniques in realistic biomedical setups remains challenging. This is especially true when the sound needs to travel through complex layers, such as the human skull, with minimum distortion at MHz frequencies [38–40].

In this study, we propose a space-coiling metamaterial to enhance ultrasound transmission through an aberration layer, effectively enhancing the overall transmission and eliminating wave distortions caused by the aberrating layer. It is shown that these metamaterials exhibit negative effective properties within specific bands, and higher transmission is achieved through the interaction between layers with negative and positive properties. These results are further improved through iterative optimization of the space-coiling structure. This improvement is expected to significantly boost both imaging clarity and therapeutic precision where ultrasound waves need to propagate through aberration layers. Compared with previous works, our design incorporates realistic material properties and boundary conditions, bringing it a step closer to real-world applications. Through a systematic design approach, our metamaterial exhibits a compact profile and can operate at a higher frequency range by relaxing the fabrication challenges, making it better suited for practical use. The effectiveness of the proposed metamaterial is demonstrated through numerical simulations based on finite element analysis. In addition, the feasibility of the design is further validated through experimental measurements on a scaled-up prototype fabricated using fused silica. It is hoped that our proposed metamaterial will facilitate ultrasound imaging and treatment applications in the MHz range, where aberration layers, such as skull and calcified plaque, are present. To provide a broader context, a detailed comparison of existing approaches is shown in Table S1.

2 | Results

2.1 | Transmission Characterization

To begin with, we consider 1D ultrasound wave propagation through the aberrating layer, allowing for the analysis of pressure distributions and wave interactions within the modeled domain.

Figure 1 illustrates the configurations used to analyze acoustic wave propagation through the aberration layer and the proposed space-coiling metamaterial. Without loss of generality, aberration layer is considered to be Yellow 20, which is commonly used as an ultrasound phantom to mimic human skulls [6, 20]. The aberration layer is immersed in water, and the acoustic impedance of the Yellow 20 is four times larger than the background medium, which indicates strong reflection and potential for significant aberration of acoustic waves at the interface, as shown in Figure 1a left. In contrast, Figure 1a right shows the configuration where a space-coiling metamaterial is placed adjacent to the aberration layer, with both

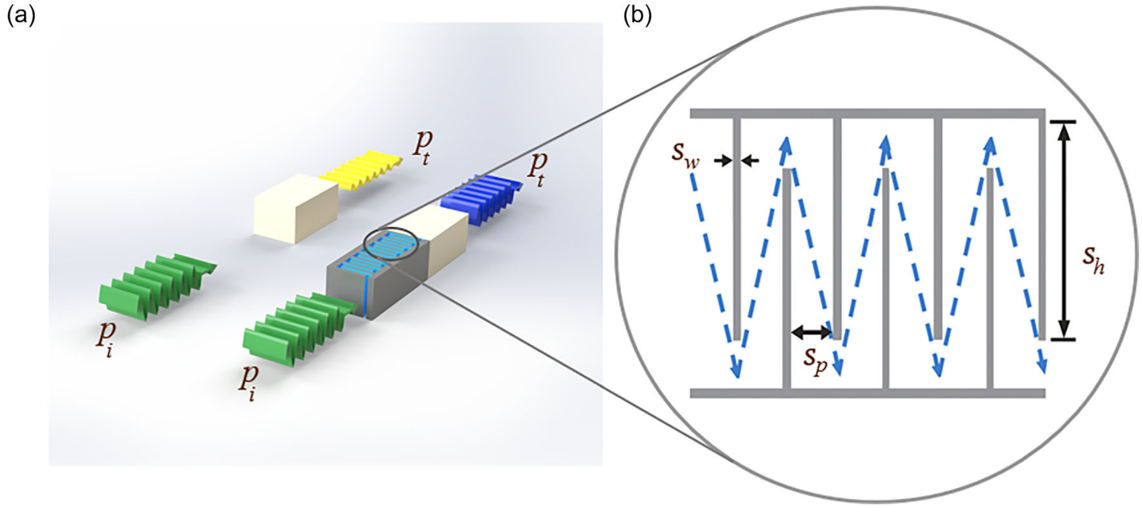

FIGURE 1 | (a) Conceptual illustration of the space-coiling metamaterial for enhanced ultrasound transmission through the aberration layer. When the metamaterial is absent, the transmission is low due to a strong impedance mismatch (left). When the metamaterial is placed adjacent to the aberration layer, the transmission is increased by harnessing the interactions between them (right). (b) Zoom-in view of the metamaterial unit cell, highlighting the geometric parameters, segment width s_w, spacing s_p, and height s_h.

components immersed in water. In this work, the seven-wall configuration shown in Figure 1b serves as a single metamaterial unit cell. The number of walls was chosen to balance extending the wave path for enhanced wave–structure interaction, while maintaining sufficient channel width for manufacturability. The structure is made of steel, which provides high acoustic impedance and structural rigidity necessary for efficient wave guidance and reflection. The space-coiling configuration enables acoustic waves to pass through the thin channels formed by the steel plates, creating controlled resonant behavior that can help enhance acoustic transmission, which will be shown later. The sound attenuation effect of the aberration layer, adjacent to the space-coiled metamaterial, is numerically investigated using the pressure acoustics module in COMSOL Multiphysics. A frequency-domain study has been set up to examine transmission through the proposed space-coiled metamaterial. The simulation geometry includes a coiled internal channel within a rectangular waveguide with a cross-sectional size of 2×0.06 mm. Waves are incident from the left side, and the coefficient is extracted by taking the average absolute pressure on the outlet boundary at the right end of the waveguide. The upper and lower boundaries of the waveguide domain are sound-hard walls to ensure plane wave propagation. The unit cell walls are modeled as interior sound-hard boundaries to mimic rigid walls. The propagation medium is filled with water of density $\rho = 1000$ kg/m^3 and speed of sound $c = 1500$ m/s. Acoustic material properties are assigned to the aberration layer and metamaterial domains in COMSOL Multiphysics.

The computational domain is discretized using a triangular finite element mesh with a maximum element size of $\lambda/6$, ensuring a sufficient number of elements per wavelength in the acoustic medium. Convergence analysis confirmed that the transmission results remained unchanged with further mesh refinements, indicating numerical stability. The metamaterial exhibits high transmission owing to resonant tunneling effects that compensate for aberrations introduced by the layer, thereby enhancing its overall transmission characteristics.

The geometric configuration of the space-coiling metamaterial is parameterized by the segment height s_h, the segment width s_w, and the separation between adjacent segments s_p as shown in the zoom-in view of the metamaterial unit cell in Figure 1b. To determine how the geometry of the space-coiling metamaterial influences its acoustic behavior, an iterative process is conducted by varying three key design variables: segment width s_w, segment spacing s_p, and segment height s_h, while an aberration layer made of yellow 20, equal in size to the metamaterial, is placed next to it. The corresponding transmission spectra are shown in Figure 2, showing evident resonance peaks within the frequency range between 1 and 6 MHz under different values of s_w, s_p, and s_h, respectively. As shown in Figure 2a, the transmission behavior is periodic with respect to the channel width s_w. Within each frequency range (e.g., 1–3 MHz or 3–5 MHz), increasing s_w from 0.0025 to 0.009 mm shifts the resonance peaks toward lower frequencies, while simultaneously narrowing the bandwidth of each transmission maximum. This trend indicates that larger s_w values enhance the impedance mismatch and scattering efficiency, leading to more pronounced attenuation bands.

Figure 2b depicts the effect of altering the s_p from 0.006 to 0.04 mm. It is evident that increasing s_p tends to broaden the bandwidths of the attenuation regions and introduces more complex transmission behavior. The unit cells are tightly coupled at lower s_p values, leading to narrower bandgaps. In contrast, larger spacings produce more distributed and overlapping resonance features. In Figure 2c, the segment height s_h varies across a broad range from 0.01 to 0.58 mm. A decrease in s_h corresponds to increased transmission at low frequencies and weaker resonance behavior, while increasing s_h intensifies the attenuation and shifts the resonance peaks toward higher frequencies. This suggests that s_h mainly affects the vertical confinement of the acoustic field and contributes to mode shaping within the metamaterial unit. Overall, these results demonstrate that the acoustic transmission properties of the space-coiling metamaterial can be precisely tuned through careful adjustment of its geometric parameters.

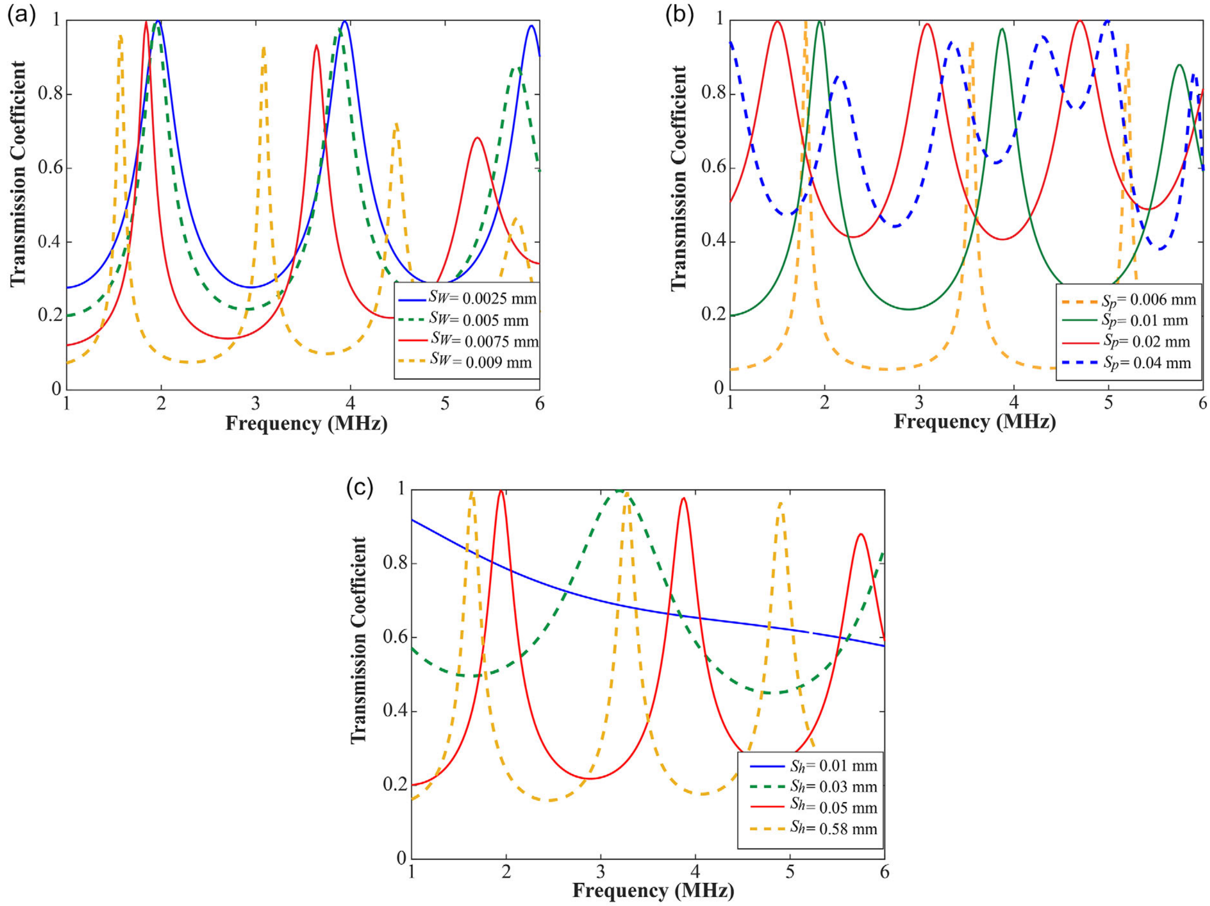

FIGURE 2 | Transmission spectra of the space-coiling metamaterial under different geometric configurations: (a) effect of segment width s_w, (b) effect of segment spacing, and (c) effect of segment height s_h.

On the other hand, the resonance behavior persists across different thickness ratios between the aberration layer and the metamaterial. This property facilitates practical design and implementation, as a relatively thin metamaterial layer can be employed to enhance transmission through a much thicker aberration layer. To investigate the influence of aberration-layer thickness on wave transmission, numerical simulations are conducted for configurations consisting of a single metamaterial unit cell paired with aberration layers of varying lengths. The aberration layer is assigned lengths equal to 0.5×, 1×, 2×, and 3× the length of the metamaterial structure, as shown in Figure 3a–d. As shown in Figure 3, despite the different thickness ratios, resonance peaks are observed in all the cases. On the other hand, more well-defined and pronounced peaks are observed with a smaller ratio, and decreased transmission is observed with a larger ratio. While changing the thickness of the layers shifts the transmission patterns, the underlying mechanism, i.e., the resonance phenomenon, remains. In real-world scenarios such as ultrasound imaging or therapy through the skull, the aberration layer may exhibit variations in its profile and is patient-specific. To accommodate this, the detailed property of the skull could be first obtained via appropriate imaging techniques such as CT scans. The thickness as well as the number of the metamaterial unit cell can then be adjusted to form a conformal profile to ensure high transmission through the skull, specific for each case [41].

2.2 | Design and Analysis of the Metamaterial Unit Cell

The mathematical model of the space-coiling metamaterial can be understood based on how waves travel within each small channel. Due to the geometry of the structure, the effective acoustic path length is significantly larger than the physical thickness of the unit cell. As a result, the accumulated phase delay can be expressed as

$$\phi = kL_{\text{eff}} \tag{1}$$

where ϕ is the phase delay, k is the acoustic wavenumber, and L_{eff} is the effective propagation length inside the coiled channel. This increased phase accumulation enables strong control over wave propagation within a compact structure. Furthermore, the transmission characteristics of the metamaterial are governed by resonance effects associated with the coiled paths. The resonance frequencies can be approximated by

$$f_n \approx \frac{nc}{2L_{\text{eff}}} \tag{2}$$

where f_n is the resonance frequency of order n, c is the speed of sound in the medium, and L_{eff} is the effective acoustic path length [42, 43].

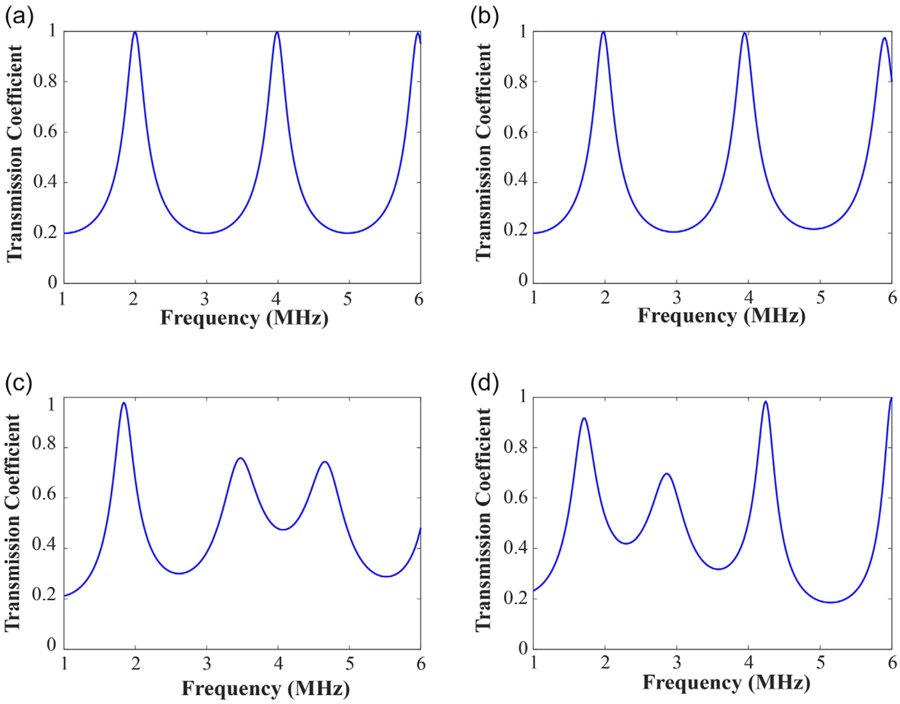

FIGURE 3 | Transmission spectra of the metamaterial structure consisting of a single unit cell combined with aberration layers of varying lengths: (a) aberration layer length = 0.5× metamaterial length, (b) aberration layer length = 1× metamaterial length, (c) aberration layer length = 2× metamaterial length, and (d) aberration layer length = 3× metamaterial length.

However, directly applying these models in the present study is challenging because of the geometric complexity involved in the parametric design of the coiled-space structure. In addition, this work operates in the resonant regime of space-coiling metamaterials, which is highly sensitive and deviates from the assumptions underlying the analytical models developed for nonresonant conditions. Therefore, a numerical modeling approach was adopted and systematically optimized through iterative variation of the geometric parameters.

The optimization of the space-coiling metamaterial is carried out by systematically varying three structural parameters: s_w, s_p, and s_h. This is done by the Live Link with MATLAB module of COMSOL Multiphysics that allows parametric studies by changing geometric features in one or multiple for loops. To this aim, a base COMSOL simulation file was set up with a coiled space geometry and parametrized s_w, s_p, and s_h. In three nested loops, these parameters varied over the ranges shown in Table 1, ensuring that the structure is physically realizable.

TABLE 1 | Parameter sweep ranges are used in the optimization study. All geometric parameters are normalized by the wavelength at the target frequency of 4 MHz.

Parameter	Range (normalized by $\lambda_{4\,\mathrm{MHz}}$)	Step (normalized by $\lambda_{4\,\mathrm{MHz}}$)
s_w	[0.0080, 0.0186]	0.00266
s_h	[0.0266, 0.1466]	0.0133
s_p	[0.0161, 0.0960]	0.0133

Where λ_{MHz} denotes the wavelength at the target frequency 4 MHz, which is a typical frequency used in diagnostic applications, especially for tissue and blood flow imaging. A total of 350 parameter combinations were evaluated, and among these configurations, the structure consisting of a single unit cell with parameters $s_w = 0.004$ mm, $s_p = 0.016$ mm, and $s_h = 0.035$ mm exhibits a pronounced enhancement in acoustic transmission at 4 MHz. As shown in Figure 4a, the presence of only the aberration layer yields a transmission amplitude of ≈0.52 at 4 MHz. However, when a space-coiling metamaterial is introduced adjacent to the aberration layer whose thickness is 2.5 times that of the metamaterial, the transmission increases remarkably, reaching a value of 0.97, as shown in Figure 4b. The bandwidth of the transmission peak in the optimal coiled space is also desirable at a value of 4 MHz, avoiding a sharp peak that could make the design highly sensitive to fabrication errors.

To gain further insight into the resonance behavior of the metamaterial, its effective properties are analyzed. It should be noted that the retrieval of effective acoustic parameters, including the effective mass density and bulk modulus, is based on the homogenization assumption that the acoustic wavelength is sufficiently larger than the characteristic dimensions of the metamaterial unit cell. Under this condition, the structured medium can be approximated as an equivalent homogeneous material with frequency-dependent effective properties. The dimension of our designed metamaterial unit cell is 0.1 mm, well below the corresponding wavelength at around 4 MHz. The effective refractive index n and the normalized acoustic impedance ξ are retrieved from the simulated reflection (R) and transmission (T) coefficients using the standard inversion method, where k is the wavenumber, d is the slab thickness, and m is the branch index [36, 44, 45].

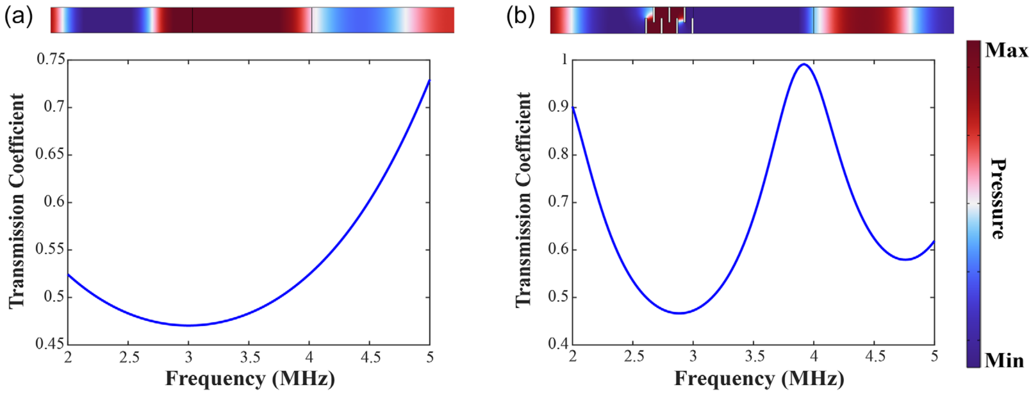

FIGURE 4 | Transmission spectra of the layered structures: (a) background medium with an embedded aberration layer, and (b) configuration in which a space-coiling metamaterial is introduced adjacent to the aberration layer. The frequency for the pressure plots is 4 MHz.

$$n = \frac{-i}{kd} \ln(x) + \frac{2\pi m}{kd} \tag{3}$$

$$\xi = \sqrt{\frac{(1+R)^2 - T^2}{(1-R)^2 - T^2}} \tag{4}$$

where

$$x = \frac{1 - R^2 + T^2 + r}{2T}, \qquad r = \sqrt{(R^2 - T^2 - 1)^2 - 4T^2} \tag{5}$$

Finally, the equivalent effective mass density and bulk modulus are expressed as

$$\rho_{\text{eff}} = \xi n \tag{6}$$

$$B_{\text{eff}} = \frac{\xi}{n} \tag{7}$$

As shown in Figure 5, the effective mass density (ρ_{eff}) and the effective bulk modulus (B_{eff}) are negative values within the frequency ranges [2.74, 5.44] MHz and [2.8, 5.24] MHz, respectively. The emergence of such negative effective properties at these frequency ranges indicates that the space-coiling metamaterial functions as a complementary medium to the aberration layer. Consequently, the aberration effects are effectively compensated, resulting in a pronounced enhancement of acoustic transmission [4, 46, 47].

As previously demonstrated, changing the thickness ratio between the aberration layer and the metamaterial provides a way to precisely control the frequency at which enhanced acoustic transmission occurs. In the updated design, the thickness of the aberration layer was set equal to that of the metamaterial to reestablish the transmission enhancement at 4 MHz. In this step, the space-coiling metamaterial was redesigned by adjusting the geometric parameters, such as s_w, s_p, and s_h, to achieve maximum transmission at the target frequency. To further understand the interaction between the metamaterial and the propagating acoustic waves, the simulated pressure fields were examined at 1.5, 2.5, 3.5, and 4 MHz, as shown in Figure 6. Notably, the configuration with a single unit cell ($s_w = 0.007$ mm, $s_p = 0.036$ mm, and $s_h = 0.055$ mm) exhibited a pronounced improvement in acoustic transmission, reaching $T = 0.99$ at 4 MHz. At the lowest frequency (1.5 MHz), the acoustic field propagated almost unaffected, indicating negligible interaction with the structure. At 2.5 MHz, the field pattern began to distort, and interference effects emerged, signifying the onset of coupling between the incident wave and the coiling geometry. At 3.5 MHz, the transmitted field weakened due to increased scattering and phase accumulation. The behavior became much more prominent at 4 MHz, where energy was strongly confined within the coiling paths. This condition corresponds to a resonance state, characterized by energy localization inside the structure, enabling more efficient wave manipulation and a marked increase in transmission through the aberrating layer.

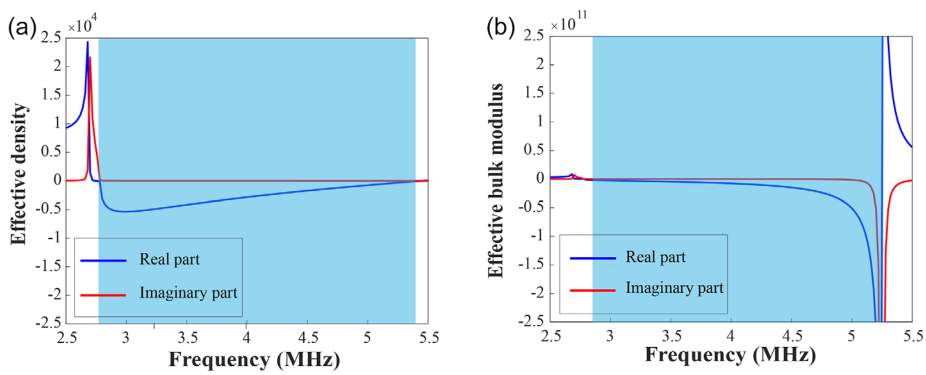

FIGURE 5 | (a) The equivalent mass density ρ_{eff} (kg/m^3). (b) The equivalent bulk modulus B_{eff} (Pa) of the space-coiling metamaterial. The highlight blue shadings indicate the frequency ranges with negative values for effective properties.

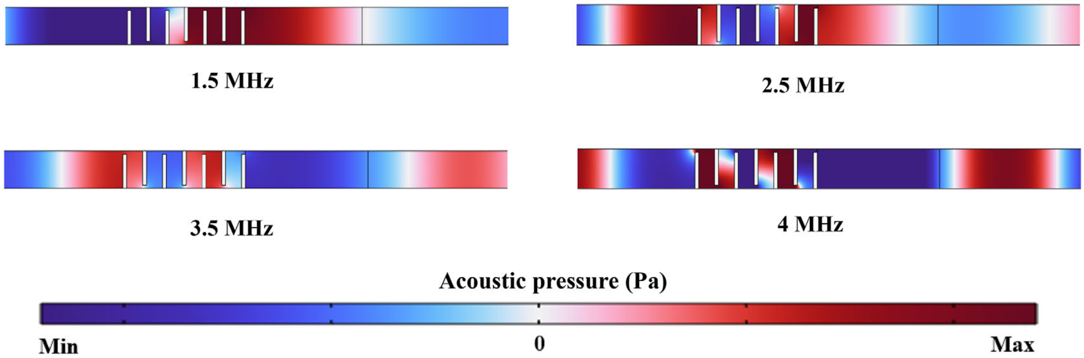

FIGURE 6 | The acoustic pressure fields of the space-coiling metamaterial and aberration layer under different frequencies.

An important feature of the proposed unit cell design is its scalability. The number of patterned unit cells and the overall thickness of the metamaterial layer can be tailored to match different aberration layer thicknesses. This approach demonstrates not only a parametric flexibility but, more importantly, confirms that the concept remains effective across a range of configurations. To assess the impact of unit cell quantity on the acoustic performance of the space-coiling metamaterial layer, a parametric study was conducted using configurations with one-, two-, four-, and ten-unit cells. The corresponding transmission spectra are shown in Figure 7, where subfigures (a) to (d) illustrate the frequency response for these four configurations, respectively. In all configurations, the thickness of the aberration layer is set equal to the thickness of the metamaterial, maintaining a consistent overall structural length for comparative analysis. Apart from a minor frequency shift or small design adjustments, the transmission enhancement is preserved, indicating that the same design strategy can be readily adapted to diverse practical scenarios.

As shown in Figure 7a, the metamaterial composed of a single unit cell exhibits a limited number of distinct transmission dips corresponding to isolated resonance modes. With the introduction of two-unit cells (Figure 7b), additional features appear in the transmission spectrum, reflecting the initial effects of inter-cell interactions and the emergence of coupled resonant modes. The resulting attenuation regions broaden slightly, indicating improved impedance mismatch and localized wave trapping. Increasing the number of unit cells to four is shown in Figure 7c, leading to a noticeable change in the transmission

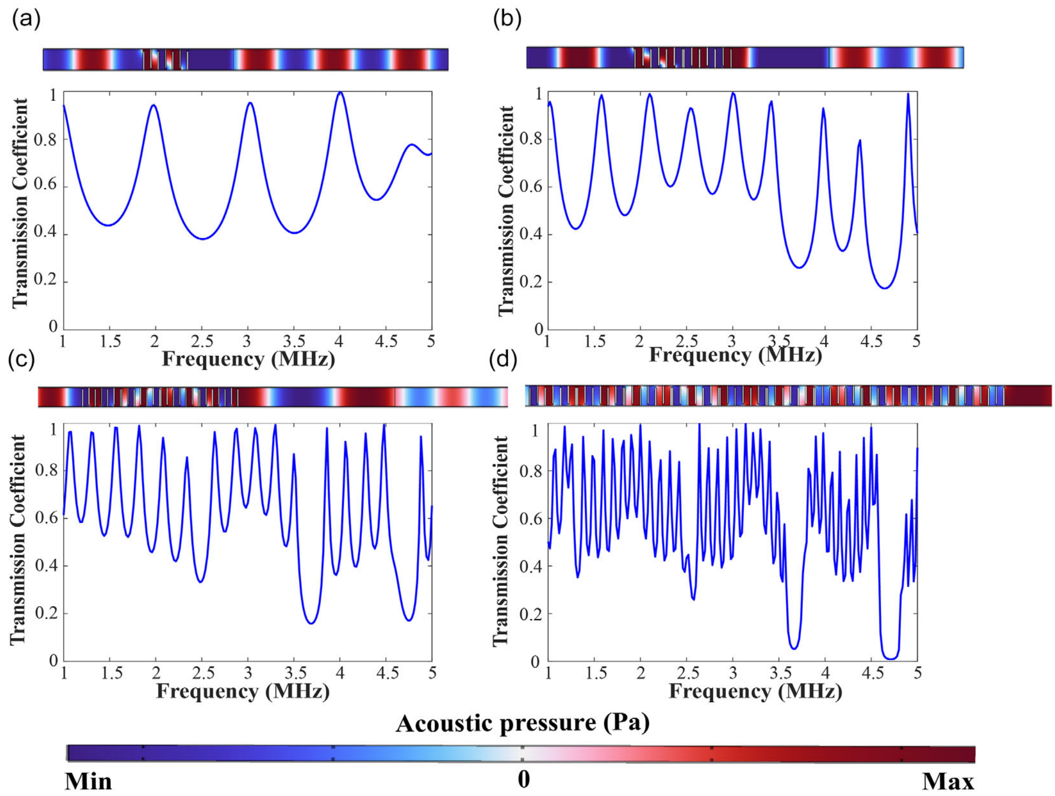

FIGURE 7 | Transmission spectra of the metamaterial structure with varying numbers of unit cells in the metamaterial layer: (a) one-unit cell, (b) two-unit cells, (c) four-unit cells, and (d) ten-unit cells at 4 MHz. The size of the metamaterial is equal to the size of aberration layer. The pressure plots in (a–d) are shown at 4 MHz.

profile, yielding a denser distribution of sharp resonant notches across a wider frequency range. This happens due to the increased periodicity, which strengthens constructive and destructive interference, resulting in the formation of multiple stop bands. When the unit cell numbers reach ten (Figure 7d), the transmission response becomes highly intricate, characterized by a quasiperiodic sequence of deep transmission dips and extended bandgaps. This indicates strong multiple scattering, effectively suppressing wave propagation over a broad frequency range. Overall, an increase in the number of unit cells leads to additional resonance dips, wider attenuation bands, and more complex transmission behavior. While the design and optimization are performed at the unit cell level, the overall thickness of both the metamaterial and aberration layers can be adjusted by patterning additional unit cells or modifying the length of the aberration layer.

3 | Potential Implementation with Realistic Materials

We conducted a detailed optimization study using a single fused silica unit cell placed adjacent to an aberration layer with a thickness 2.5 times greater than that of the metamaterial. Since fused silica is not acoustically rigid, the model did not include a sound-hard boundary condition. Such treatment also relaxes the assumption of acoustically rigid boundaries in many space-coiling metamaterials and represents one step further toward their practical implementation. After evaluating 605 parameter combinations, we identified an optimal geometry with a segment width of $s_w = 0.003$ mm, spacing of $s_p = 0.026$ mm, and a height of $s_h = 0.05$ mm, achieving a maximum simulated transmission of 0.94 at 4 MHz, as shown in Figure 8.

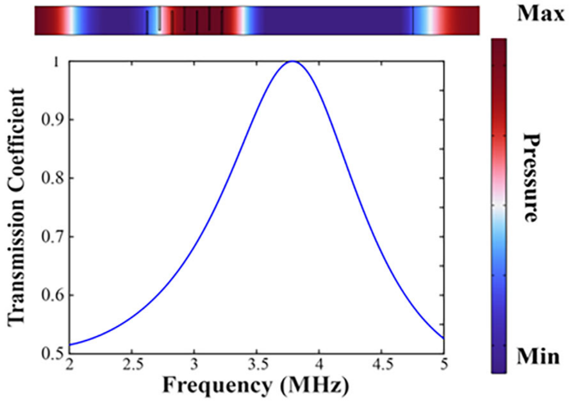

FIGURE 8 | Transmission spectra of the layered structure incorporating a fused silica space-coiling metamaterial.

Our simulations show that these space-coiling designs work effectively by boosting ultrasound transmission through mismatched barriers. However, their manufacturing could be difficult because of the small feature size and material availability. To demonstrate the potential application of the space-coiling metamaterial, we showcase the fabrication of a prototype of a unit cell using fused silica, a material compatible with high-resolution techniques. The prototype is scaled up ten times larger than our original model to relax the resolution constraints. By using a femtosecond laser to write the design and then chemically etching away the extra parts, we can fine-tune structures with precise, smooth internal channels [48]. Due to the limitations of current fabrication technologies, minor modifications were made to the design, including slight adjustments to the wall thickness and channel layout, to ensure that all key features are well resolved and that the structure remains mechanically stable during manufacturing, as shown in Figure 9a.

To show the potential usage of the proposed metamaterial, we performed measurements in a water tank using a pair of ultrasonic transducers in a transmission configuration. The incident acoustic waves passed through the metamaterial, and the transmitted signal was recorded on the opposite side. The transmission coefficient was obtained by normalizing the measured signal with respect to a reference measurement without the sample, as shown in Figure 9b. A pronounced transmission peak is observed around 450 kHz, indicating a strong resonance due to the presence of the metamaterial. This shift to lower frequencies is consistent with geometric scaling, as the operating frequency is inversely proportional to the

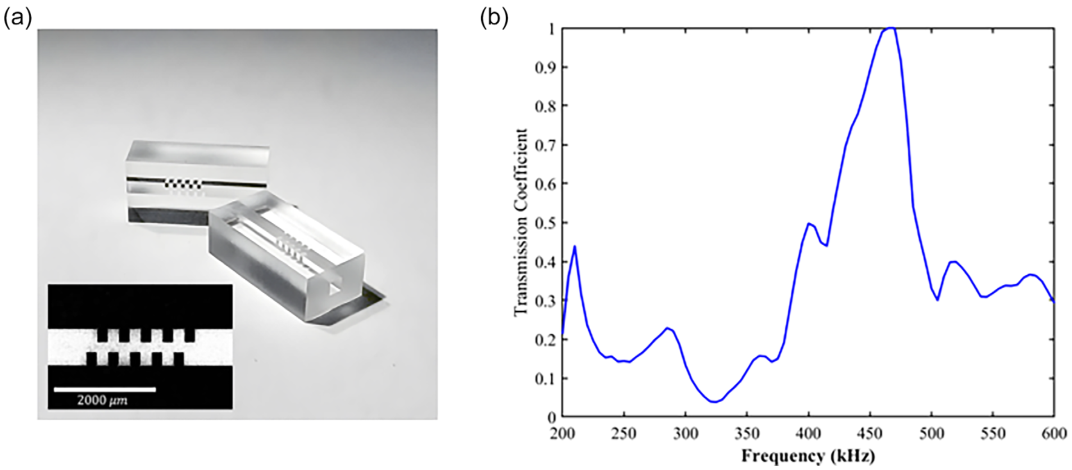

FIGURE 9 | (a) 3D-printed models of the fused silica space-coiling structure, and (b) measured transmission spectrum of the layered system incorporating the fused silica metamaterial.

characteristic dimensions of the unit cell. Importantly, the experimental results exhibit the same qualitative behavior as predicted by numerical simulations, including a desirable bandwidth around the transmission peak, confirming that the underlying mechanisms of transmission enhancement, namely, resonant tunneling and impedance compensation, remain valid across different scales.

4 | Discussion

The proposed space-coiling metamaterial shows strong potential for mitigating the impedance mismatch introduced by aberrating layers such as skull or arterial phantoms. It should also be noted that these simulations were created with water as the background medium. In reality, biomedical applications would most likely use multilayered tissues with different acoustic impedance and attenuation. This could lead to further reflection and energy loss and may be mitigated by incorporating a multilayer design approach, where the metamaterial contains multiple layers that are each designed with specific parameters to improve the transmission through the corresponding aberration layer. One of the major challenges, however, lies in fabrication. The design requires micron-scale features that, within the scope of this work, could not be realized with available techniques. Approaches, such as high-resolution 3D printing or laser-based microfabrication, may offer a path forward. Nevertheless, current fabrication technologies face two key limitations: achieving the subwavelength resolution necessary for acoustic metamaterial features and processing stiff materials with sufficient mechanical rigidity and acoustic impedance. These challenges highlight the broader difficulty of translating acoustic metamaterial concepts from numerical design to experimental realization. Even so, our simulations substantiate that the space-coiling geometry can effectively reduce impedance mismatch and enhance transmission, leading to measurable improvements in acoustic performance. The enhancement observed in the MHz range is particularly promising for ultrasound imaging and therapeutic applications.

To further demonstrate the feasibility of the proposed concept, a scaled-up prototype was fabricated and experimentally tested. The experimental results show a clear transmission peak around 450 kHz, suggesting the presence of strong resonance. Although this frequency differs from the MHz regime of the simulations due to geometric scaling, the observed behavior is consistent with the predicted transmission mechanism. This agreement confirms that the underlying physics of resonant tunneling and impedance compensation remain valid across different scales, providing experimental support for the simulation-based findings. Looking ahead, continued progress in fabrication methods, along with further optimization and full-scale experimental validation, will be essential for translating these concepts into practical biomedical devices.

5 | Conclusion

In conclusion, this work demonstrates that space-coiling metamaterials can significantly enhance ultrasound transmission through layers that typically block or distort acoustic waves. Furthermore, using numerical simulation, fused silica is shown to be a suitable material to realize such a metamaterial. A fabricated sample is demonstrated, providing evidence for the feasibility of this technique in practice. These findings lay the groundwork for future experimental studies and point toward eventual applications in medical imaging and therapeutic ultrasound treatments by adjusting the structural parameters and placing an optimally designed metamaterial layer between the imaging probe and the aberration layer, where correcting aberrations and improving penetration are critical [49, 50]. In the future, focus will be on testing the performance of the full-scale fabricated metamaterials and possible ways by which such a structure can be implemented in a linear-array probe.

Acknowledgments

M.G. and C.S. were supported by the National Science Foundation under Grant No. CBET-2243507. A.G.D. was supported by a ZonMw grant from the Dutch government. We thank LightFab GmbH (Germany), in particular Claudia Preußker, for fabricating the test samples free of charge, and Ehasan Heshmati (University of Twente) for photographing the samples.

Funding

This study was supported by National Science Foundation (Grant CBET-2243507) and the Netherlands Organisation for Health Research and Development (ZonMw) under the OffRoad grant scheme (Grant No. 04510012210058).

Conflicts of Interest

The authors declare no conflicts of interest.

Data Availability Statement

The data that support the findings of this study are available from the corresponding author upon reasonable request.

References

1. T. Chen, J. Chen, Z. Yi, et al., "Enhanced Ultrasound Transmission Through Skull Using Flexible Matching Layer With Gradual Acoustic Impedance," *ACS Applied Materials & Interfaces* 15, no. 48 (2023): 55510–55517, https://doi.org/10.1021/acsami.3c13872.

2. R. You, H. Wu, W. Pang, and X. Duan, "On-Chip Arbitrary Manipulation of Single Particles by Acoustic Resonator Array," *Analytical Chemistry* 94, no. 13 (2022): 5392–5398, https://doi.org/10.1021/acs.analchem.2c00130.

3. Y. Wu and Y. Meng, "Cell Manipulation and Single Cell Characterization on Microfluidic Devices," *TrAC Trends in Analytical Chemistry* 168 (2023): 117301, https://doi.org/10.1016/j.trac.2023.117301.

4. J. Wang, F. Allein, N. Boechler, J. Friend, and O. Vazquez-Mena, "Design and Fabrication of Negative-Refractive-Index Metamaterial Unit Cells for Near-Megahertz Enhanced Acoustic Transmission in Biomedical Ultrasound Applications," *Physical Review Applied* 15, no. 2 (2021): 024025, https://doi.org/10.1103/PhysRevApplied.15.024025.

5. S. R. Craig, P. J. Welch, and C. Shi, "Non-Hermitian Complementary Acoustic Metamaterials for Lossy Barriers," *Applied Physics Letters* 115, no. 5 (2019): 051902, https://doi.org/10.1063/1.5110501.

6. C. Shen, J. Xu, N. X. Fang, and Y. Jing, "Anisotropic Complementary Acoustic Metamaterial for Canceling Out Aberrating Layers," *Physical Review X* 4, no. 4 (2014): 041033, https://doi.org/10.1103/PhysRevX.4.041033.

7. E. Dong, T. Zhang, J. Zhang, et al., “Soft Metalens for Broadband Ultrasonic Focusing Through Aberration Layers,” *Nature Communications* 16, no. 1 (2025): 308, https://doi.org/10.1038/s41467-024-55022-2.

8. P. Das, J. Gupta, D. Sikdar, and R. Bhattacharjee, “Aperture–patch Sandwich Metasurface for Magnetic Field Enhancement in 1.5 T MRI,” *Magnetic Resonance Imaging* 100 (2023): 1–9, https://doi.org/10.1016/j.mri.2023.03.005.

9. P. Das, J. Gupta, D. Sikdar, and R. Bhattacharjee, “A Non-Linear Triangular Split-ring Based Metaresonator for Targeted Scanning at 1.5 T MRI,” *Physica Scripta* 98, no. 6 (2023): 065004, https://doi.org/10.1088/1402-4896/accf49.

10. C. Demené, J. Robin, A. Dizeux, et al., “Transcranial Ultrafast Ultrasound Localization Microscopy of Brain Vasculature in Patients,” *Nature Biomedical Engineering* 5, no. 3 (2021): 219–228, https://doi.org/10.1038/s41551-021-00697-x.

11. T. S. Riis, T. D. Webb, and J. Kubanek, “Acoustic Properties Across the Human Skull,” *Ultrasonics* 119 (2022): 106591, https://doi.org/10.1016/j.ultras.2021.106591.

12. M. van Helvert, S. Engelhard, J. Voorneveld, et al., “High-Frame-Rate Contrast-Enhanced Ultrasound Particle Image Velocimetry in Patients With a Stented Superficial Femoral Artery: A Feasibility Study,” *European Radiology Experimental* 6, no. 1, 2022, https://doi.org/10.1186/s41747-022-00278-w.

13. J. Plomp, A. Ghanbarzadeh-Dagheyan, M. Versluis, G. Lajoinie, and E. G. Jebbink, “Imaging Behind the Plaque: Improved Blood Flow Quantification Using an Iterative Scheme for Active Attenuation Correction,” *Ultrasound in Medicine & Biology* 51, no. 6 (2025): 984–998, https://doi.org/10.1016/j.ultrasmedbio.2025.02.012.

14. Y. Chen, M. Hua, T. Zhang, M. Zhou, J. Wu, and W. Zou, “Holographic Near-Eye Display Based on Complex Amplitude Modulation With Band-Limited Zone Plates,” *Optics Express* 29, no. 14 (2021): 22749–22760, https://doi.org/10.1364/OE.431032.

15. D. Andrés, A. Carrión, F. Camarena, and N. Jiménez, “Methods to Design and Evaluate Transcranial Ultrasonic Lenses Using Acoustic Holography,” *Physical Review Applied* 20, no. 4 (2023): 044071, https://doi.org/10.1103/PhysRevApplied.20.044071.

16. M. Xu, J. Wang, W. S. Harley, P. V. S. Lee, and D. J. Collins, “Programmable Acoustic Holography Using Medium-Sound-Speed Modulation,” *Advanced Science* 10, no. 23 (2023): 2301489, https://doi.org/10.1002/advs.202301489.

17. Z. Jia, J. Li, C. Shen, Y. Xie, and S. A. Cummer, “Systematic Design of Broadband Path-Coiling Acoustic Metamaterials,” *Journal of Applied Physics* 123, no. 2 (2018): 025101, https://doi.org/10.1063/1.5009488.

18. J. Zhao, Z. Li, C. Fei, et al., “Ultrawide Bandwidth High-Frequency Ultrasonic Transducers With Gradient Acoustic Impedance Matching Layer for Biomedical Imaging,” *IEEE Transactions on Ultrasonics, Ferroelectrics, and Frequency Control* 69, no. 6 (2022): 1952–1959, https://doi.org/10.1109/TUFFC.2022.3141203.

19. K. Zhu, J. Ma, X. Qi, et al., “Enhancement of Ultrasonic Transducer Bandwidth by Acoustic Impedance Gradient Matching Layer,” *Sensors* 22, no. 20 (2022): 8025, https://doi.org/10.3390/s22208025.

20. A. Ghanbarzadeh-Dagheyan, E. Dong, and N. X. Fang, “A Meta Matching Layer to Image Behind Calcified Plaques,” 2024 IEEE Ultrasonics, Ferroelectrics, and Frequency Control Joint Symposium (UFFC-JS), (IEEE, 2024), 1–6, https://doi.org/10.1109/UFFC-JS60046.2024.10793787.

21. L.-J. Xu, L. Zhu, and M. Liang, “Impedance Matching at Skin–air Interface for Transmission-Range Improvement of Implantable Antennas,” *IEEE Transactions on Antennas and Propagation* 71, no. 3 (2023): 2235–2246, https://doi.org/10.1109/TAP.2023.3234180.

22. V. T. Rathod, “A Review of Acoustic Impedance Matching Techniques for Piezoelectric Sensors and Transducers,” *Sensors* 20, no. 14 (2020): 4051, https://doi.org/10.3390/s20144051.

23. Q. Lu, X. Li, X. Zhang, M. Lu, and Y. Chen, “Perspective: Acoustic Metamaterials in Future Engineering,” *Engineering* 17 (2022): 22–30, https://doi.org/10.1016/j.eng.2022.04.020.

24. G. Aydın and S. E. San, “Breaking the Limits of Acoustic Science: A Review of Acoustic Metamaterials,” *Materials Science and Engineering: B* 305 (2024): 117384, https://doi.org/10.1016/j.mseb.2024.117384.

25. Q. Deng, T. Du, H. Gomaa, Y. Cheng, and C. An, “Methods of Manipulation of Acoustic Radiation Using Metamaterials With a Focus on Polymers: Design and Mechanism Insights,” *Polymers* 16, no. 17 (2024): 2405, https://doi.org/10.3390/polym16172405.

26. P. Das, J. Gupta, D. Sikdar, and R. Bhattacharjee, “A Smart Metasurface for Scanning Deep Brain Tissues at 1.5 T MRI,” *Current Applied Physics* 53 (2023): 172–180, https://doi.org/10.1016/j.cap.2023.07.003.

27. Y. Deng and C. Shi, “Active Non-Hermitian Complementary Acoustic Metamaterials for Transcranial Imaging,” *The Journal of the Acoustical Society of America* 155, no. 3_Supplement (2024): A55–A55, https://doi.org/10.1121/10.0026782.

28. S. R. Craig, P. J. Welch, and C. Shi, “Non-Hermitian Complementary Acoustic Metamaterials for Imaging Through Skull With Imperfections,” *Frontiers in Mechanical Engineering* 6 (2020): 55, https://doi.org/10.3389/fmech.2020.00055.

29. S. B. Gebrekidan, M. Eser, M. Maeder, and S. Marburg, “Improving Absorption Performance of Resonant Metamaterials Using Self-Complementary Shapes,” *Applied Physics Letters* 123, no. 17 (2023): 171701, https://doi.org/10.1063/5.0173635.

30. L. Li, Y. Diao, H. Wu, and W. Jiang, “Complementary Acoustic Metamaterial for Penetrating Aberration Layers,” *ACS Applied Materials & Interfaces* 14, no. 25 (2022): 28604–28614, https://doi.org/10.1021/acsami.2c06227.

31. J. Guo, Y. Fang, R. Qu, and X. Zhang, “Development and Progress in Acoustic Phase-Gradient Metamaterials for Wavefront Modulation,” *Materials Today* 66 (2023): 321–338, https://doi.org/10.1016/j.mattod.2023.04.004.

32. J. Gupta, P. Das, R. Bhattacharjee, and D. Sikdar, “Resonating Sub-Wavelength Metallic Wires Based Pads for Boosting Signal-to-Noise Ratio of Birdcage Head Coils at 1.5 T MRI,” *Results in Physics* 53 (2023): 106972, https://doi.org/10.1016/j.rinp.2023.106972.

33. P. Sun, S. Xu, X. Wang, et al., “Sound Absorption of Space-Coiled Metamaterials With Soft Walls,” *International Journal of Mechanical Sciences* 261 (2024): 108696, https://doi.org/10.1016/j.ijmecsci.2023.108696.

34. G. J. Jeon and J. H. Oh, “Elastic Coiling-up-Space Metamaterial,” *Physical Review Applied* 16, no. 6 (2021): 064016, https://doi.org/10.1103/PhysRevApplied.16.064016.

35. T. Chen, C. Wang, and D. Yu, “Pressure Amplification and Directional Acoustic Sensing Based on a Gradient Metamaterial Coupled With Space-Coiling Structure,” *Mechanical Systems and Signal Processing* 181 (2022): 109499, https://doi.org/10.1016/j.ymssp.2022.109499.

36. L. Xiang, G. Wang, and C. Zhu, “Controlling Sound Transmission by Space-Coiling Fractal Acoustic Metamaterials With Broadband on the Subwavelength Scale,” *Applied Acoustics* 188 (2022): 108585, https://doi.org/10.1016/j.apacoust.2021.108585.

37. X. Jia, Y. Li, Y. Zhou, M. Hong, and M. Yan, “Wide Bandwidth Acoustic Transmission via Coiled-up Metamaterial With Impedance Matching Layers,” *Science China Physics, Mechanics & Astronomy* 62 (2019): 964311, https://doi.org/10.1007/s11433-018-9365-6.

38. J. Zhang, B. Hu, and S. Wang, “Review and Perspective on Acoustic Metamaterials: From Fundamentals to Applications,” *Applied Physics Letters* 123, no. 1 (2023): 010502, https://doi.org/10.1063/5.0152099.

39. S. Chen, Y. Fan, Q. Fu, et al., "A Review of Tunable Acoustic Metamaterials," *Applied Sciences* 8, no. 9 (2018): 1480, https://doi.org/10.3390/app8091480.

40. G. Comandini, M. Ouisse, V. P. Ting, and F. Scarpa, "Architected Acoustic Metamaterials: An Integrated Design Perspective," *Applied Physics Reviews* 12, no. 1 (2025): 011340, https://doi.org/10.1063/5.0230888.

41. J.-F. Aubry, M. Tanter, M. Pernot, J.-L. Thomas, and M. Fink, "Experimental Demonstration of Noninvasive Transskull Adaptive Focusing Based on Prior Computed Tomography Scans," *The Journal of the Acoustical Society of America* 113, no. 1 (2003): 84–93, https://doi.org/10.1121/1.1529663.

42. Y. Li, G. Yu, B. Liang, et al., "Three-Dimensional Ultrathin Planar Lenses by Acoustic Metamaterials," *Scientific Reports* 4, no. 1 (2014): 6830, https://doi.org/10.1038/srep06830.

43. Y. Li, X. Jiang, R.-Q. Li, et al., "Experimental Realization of Full Control of Reflected Waves With Subwavelength Acoustic Metasurfaces," *Physical Review Applied* 2, no. 6 (2014): 064002, https://doi.org/10.1103/PhysRevApplied.2.064002.

44. V. Fokin, M. Ambati, C. Sun, and X. Zhang, "Method for Retrieving Effective Properties of Locally Resonant Acoustic Metamaterials," *Physical Review B—Condensed Matter and Materials Physics* 76, no. 14 (2007): 144302, https://doi.org/10.1103/PhysRevB.76.144302.

45. S. B. Gebrekidan, H.-J. Kim, and S.-J. Song, "Investigation of Helmholtz Resonator-Based Composite Acoustic Metamaterial," *Applied Physics a* 125, no. 1 (2019): 65, https://doi.org/10.1007/s00339-018-2323-9.

46. T.-Y. Huang, C. Shen, and Y. Jing, "Membrane-and Plate-Type Acoustic Metamaterials," *The Journal of the Acoustical Society of America* 139, no. 6 (2016): 3240–3250, https://doi.org/10.1121/1.4950751.

47. C. Liu, P. Bai, and Y. Lai, "Sound-Impenetrable Holes in Water Based on Acoustic Complementary Medium," *Europhysics Letters* 115, no. 5 (2016): 58002, https://doi.org/10.1209/0295-5075/115/58002.

48. J. Gottmann, M. Hermans, N. Repiev, and J. Ortmann, "Selective Laser-Induced Etching of 3d Precision Quartz Glass Components for Microfluidic Applications—up-Scaling of Complexity and Speed," *Micromachines* 8, no. 4 (2017): 110, https://doi.org/10.3390/mi8040110.

49. J. Chen, B. Liu, G. Peng, et al., "Achieving High-Performance Transcranial Ultrasound Transmission Through Mie and Fano Resonance in Flexible Metamaterials," *Advanced Science* 12, no. 19 (2025): 2500170, https://doi.org/10.1002/advs.202500170.

50. L. Nie, D. A. Hutchins, L. Astolfi, et al., "A Metallic Additively Manufactured Metamaterial for Enhanced Monitoring of Acoustic Cavitation-Based Therapeutic Ultrasound," *Advanced Engineering Materials* 24, no. 4 (2022): 2100972, https://doi.org/10.1002/adem.202100972.

Supporting Information

Additional supporting information can be found online in the Supporting Information section.